


# Bi<sub>(2-x)</sub>Sb<sub>x</sub>Te<sub>3</sub> Thermoelectric Composites with High Average $zT$ Values: From Materials to Devices

Zhiliang Li<sup>1,3</sup>, Xiaofeng Yang<sup>1</sup>, Qing Wang<sup>1</sup>, Hongxia Zhang<sup>1</sup>, Zhihai Ding<sup>2</sup>, Qian Cao<sup>2</sup>, Xin Qian<sup>1</sup>, Jianglong Wang<sup>1</sup>, and Shufang Wang<sup>1,3\*</sup> 

<sup>1</sup> Key Laboratory of High-Precision Computation and Application of Quantum Field Theory of Hebei Province, College of Physics Science and Technology, Hebei University, Baoding 071002, China

<sup>2</sup> Huabei Cooling Device Co., Ltd, Xianghe 065400, China

<sup>3</sup> Institute of Life Science and Green Development, Hebei University, Baoding 071002, China

\* Corresponding author, E-mail: [sfwang@hbu.edu.cn](mailto:sfwang@hbu.edu.cn)

## Abstract

(Bi,Sb)Te-based materials have drawn extensive attention for nearly two centuries as one of the most successful commercial thermoelectric (TE) materials. However, Bi<sub>(2-x)</sub>Sb<sub>x</sub>Te<sub>3</sub> composites with remarkable average figure of merit ( $zT_{avg}$ ) values are highly desired in terms of the great contribution on expanding the applying temperature ranges of the commercial devices. Herein, Bi<sub>0.35</sub>Sb<sub>1.65</sub>Te<sub>3</sub> compound with outstanding  $zT_{avg}$  value of about 1.18 (integrate from 298 to 498 K) was obtained *via* delaying the bipolar effect by precipitating multi-scale Sb<sub>2</sub>Te<sub>3</sub> inclusions. The power factor ( $PF$ ) was enhanced from  $2.1 \times 10^{-3} \text{ Wm}^{-1} \text{ K}^{-2}$  (Bi<sub>0.5</sub>Sb<sub>1.5</sub>Te<sub>3</sub>) to  $4.3 \times 10^{-3} \text{ Wm}^{-1} \text{ K}^{-2}$  (Bi<sub>0.35</sub>Sb<sub>1.65</sub>Te<sub>3</sub>) by optimizing the carrier concentration from  $1.9 \times 10^{19} \text{ cm}^{-3}$  to  $3.9 \times 10^{19} \text{ cm}^{-3}$  *via* adjusting the proportions of Bi:Sb. Correspondingly, the lattice thermal conductivities ( $\kappa_l$ ) were distinctly suppressed by the additional multiple phonon scattering resulting from the Sb<sub>2</sub>Te<sub>3</sub> precipitates. Consequently, a remarkable  $zT_{max}$  as high as  $\sim 1.35$  at 373 K was obtained in the Bi<sub>0.35</sub>Sb<sub>1.65</sub>Te<sub>3</sub> sample. The temperature difference ( $\Delta T$ , 6.0 A current) of the TE device that assembled with the commercial N-type Bi(Te,Se) ingot has reached up to 66.9 K. The high  $zT_{avg}$ ,  $zT_{max}$  and  $\Delta T$  values will further promote the commercial applications of (Bi,Sb)Te-based materials in a wide temperature range.

**Key words:** Thermoelectric performance; Average figure of merit; Bismuth telluride; Nano-inclusion; Thermoelectric device

**Citation:** Zhiliang Li, Xiaofeng Yang, Qing Wang, Hongxia Zhang, Zhihai Ding, et al. Bi<sub>(2-x)</sub>Sb<sub>x</sub>Te<sub>3</sub> Thermoelectric Composites with High Average  $zT$  Values: From Materials to Devices. *Materials Lab* 2022, 1, 220026. DOI: [10.54227/mlab.20220026](https://doi.org/10.54227/mlab.20220026)

## 1 Introduction

Thermoelectric (TE) technology can realize the reversible conversion between thermal and electric energy *via* the Seebeck effect and Peltier effect, which has attracted increasing attention in the last two centuries<sup>[1,2]</sup>. The devices based on the TE effects have been applied in the solid-state refrigeration and heat recovery fields, such as precision electronics temperature controller, medical cryogenic storage device, on-board portable refrigerator, CPU temperature controller, and radioisotope generator, and it is also expected to be applied in the internet of things sensor power supply, intelligent household device, and so on<sup>[3–5]</sup>. The power conversion efficiency ( $\eta$ ) and coefficient of performance ( $COP$ ) are governed by the dimensionless figure of merit, which is defined as  $zT = S^2\sigma T / \kappa_{tot}$ , where  $S$ ,  $\sigma$ ,  $T$ , and  $\kappa_{tot}$  are Seebeck coefficient, electrical conductivity, absolute temperature, and total thermal conductivity<sup>[6–8]</sup>. In terms of the commercial application, the high average  $zT$  ( $zT_{avg}$ ) value over the entire working temperature range is the focus in the current researches because of its ability to enhance the  $COP$ , as well as to expand the application temperature region of the devices. Generally,  $zT_{avg}$  is

defined as  $zT_{avg} = \frac{1}{T_h - T_c} \int_{T_c}^{T_h} zT dT$ , in which  $T_h$  and  $T_c$  are the limes of the given temperature range<sup>[9]</sup>. Generally, the higher  $zT_{avg}$  values are, the greater the potential for commercial use.

P-type (Bi,Sb)Te composite is one of the most successful commercial TE material at near-room temperature as one of the legs in the Bi<sub>2</sub>Te<sub>3</sub>-based devices. The power factor ( $PF = S^2\sigma$ ) of the Bi<sub>(2-x)</sub>Sb<sub>x</sub>Te<sub>3</sub> semiconductor is high due to its intrinsic low energy band gap, high carrier mobility and band degeneracy. Bi, Sb and Te are heavy elements, and the electronegativity differences between anions and cation are weak, which resulting in an intrinsic low  $\kappa_{tot}$ . Thus, the  $zT$  values of the pristine (Bi,Sb)Te compounds are as high as 0.8–1.0. In recent years,  $zT$  peak has been enhanced by several strategies, including: refining the grain sizes by powder metallurgy technology to enhance the phonon scattering, and  $zT$  values have reached up to 1.15–1.40<sup>[10–12]</sup>; Synthesizing texture polycrystals using thermal deformation to increase the “donor-like” effect and lattice defect,  $zT$  values were enhanced to 1.18–1.40<sup>[13–16]</sup>; Forming high density dislocation arrays at grain boundaries by adding excess liquated tellurium,  $zT$  values were enhanced to 1.20–1.46<sup>[17–21]</sup>; Synthesizing

Received 17 April 2022; Accepted 29 May 2022; Published online

© 2022 The Author(s). *Materials Lab* published by Lab Academic Press

nanocrystal by wet-chemical method<sup>[22–25]</sup> or melt spinning technology<sup>[26–29]</sup>,  $zT$  values were increased to 1.07–1.47 or 1.10–1.56, respectively; Preparing ingot to optimize the carrier mobility further in the zone melting method,  $zT$  values have been improved to 1.1–1.40<sup>[30–33]</sup>. Reducing the dimensions to obtained the high  $zT$  values ( $\sim 1.5$ ), and high energy conversion efficiency *via* preparing thin films<sup>[34–36]</sup>. Even so, there is still lack of attention was payed to the  $zT_{avg}$  values, and most  $zT_{avg}$  values of the stat-of-the-art studies are blow 1.0<sup>[37–40]</sup> due to the rapid decay in the  $zT$  curve at high temperature. For the commercial application, the materials with high  $zT_{avg}$  values and wide application temperature range are still desired. Moreover, the strategy to achieve the shift of  $zT_{max}$  and the corresponding mechanism on the migration of  $zT$  peaks is indistinct.

Herein, P-type  $\text{Bi}_{(2-x)}\text{Sb}_x\text{Te}_3$  composites were prepared by the mechanical alloying combining with spark plasma sintering technology. High  $zT_{avg}$  value ( $\sim 1.18$ , in the range of 298–498 K) was obtained by precipitating multi-scale  $\text{Sb}_2\text{Te}_3$  inclusions. The shift of the thermal excitation temperature was achieved by drastically adjusting the carrier concentrations *via* increasing the antisite defects. Simultaneously, the extra lattice defects that were derived from the element doping effect and  $\text{Sb}_2\text{Te}_3$  combining effect enhanced the phonon scattering in the wide-range frequency, which resulting in a reduced lattice thermal conductivity in the wide temperature range. Ultimately, the remarkable temperature difference ( $\Delta T$ ,  $\sim 66.9$  K) was obtained in the TE device that was assembled with the commercial N-type  $\text{Bi}(\text{Te},\text{Se})$  ingot. Predictably, the TE devices that were constituted by present  $\text{Bi}_{(2-x)}\text{Sb}_x\text{Te}_3$  composites can be widely used in a broaden the temperature ranges (298–498 K) with high  $COP$ .

## 2 Materials and methods

### 2.1 Synthesis and assembly

Commercial Bi, Sb, and Te powders (99.99%) were weighed according to the stoichiometries of  $\text{Bi}_{(2-x)}\text{Sb}_x\text{Te}_3$  ( $x = 1.50, 1.55, 1.65, 1.75, 1.85$ ). The raw materials were refined using a planetary ball miller in the cemented carbide jars with rotate speed of 450 r/min for 3 h. The weight ratio of ball to material was about 10 : 1, and the mixture of hydrogen and argon was filled into the jars to prevent oxidation. Then, 75 mL anhydrous ethanol solvent was injected into the jars, and the powders were milled for another 2.0 h with rotate speed of 350 r/min. The obtained colloid suspensions were dried adequately in a vacuum chamber, and then were loaded into a cemented carbide mold and consolidated by Spark Plasma Sintering (SPS) method under the uniaxial pressure of 50 MPa. The powder was sintered at 673 K for 5 min, and then heat preservation at 723 K for 5 min. After cooling, cylindrical samples with the diameter of 15.0 mm and the height of 11.0 mm were obtained. The blocks were cut into wafers with the thickness of 1.8 mm by a multi-wire cutting machine. The wafers were electroplated with nickel and tin, and then were cut into cuboids with the sizes of 1.8 mm  $\times$  1.4 mm  $\times$  1.4 mm. Copper-clad substrates were welded to both sides of the particles in the reflow oven after putting the N and P particles into a positioning mold. Finally, the electric wires were wel-

ded, and the devices were sealed with silicone rubber.

### 2.2 Structural characterization and thermoelectric property measurement

Phase structures and morphologies of the as-prepared samples were identified using the Bruker AXS D8 Advance X-ray diffractometer (XRD, with  $\text{Cu-K}\alpha$  radiation), Zeiss Ultra55 scanning electron microscope (SEM), and FEI Talos F200 field emission transmission electron microscope (FETEM, 200 kV). Temperature-dependent  $\sigma$  and  $S$  were measured by ZEM-3 (UIVAC-RIKO, Japan) in a helium environment. Hall carrier concentrations ( $n_H$ ) and mobilities ( $\mu_H$ ) were measured using a Hall measurement system based on the Van der Pauw method (ET9107-HS, East Changing Technologies, Inc., China) with 1.2 T magnetic field. The thermal diffusion coefficients ( $\lambda$ ) were evaluated by a laser flash apparatus (LFA 1000, LINSEIS, Germany) from 298 K to 498 K. The total thermal conductivities were calculated according to the formula,  $\kappa_{tot} = \lambda\rho C_v$ , in which  $\rho$  is the density determined by Archimedes' principle, and  $C_v$  is the specific heat capacity calculated by the Dulong-Petit method. The final specimens using in the test equipment were cut out from the cylindrical samples along two vertical directions, which to confirm that the transmission direction of the TE parameters, including  $\sigma$ ,  $S$ ,  $n_H$ ,  $\mu_H$ , and  $\lambda$ , all are along the direction perpendicular to the uniaxial pressure in the SPS. The maximum temperature difference ( $\Delta T_{max}$ ), working voltage ( $U_{max}$ ), maximum temperature difference of current ( $I_{max}$ ), refrigerating capacity ( $Q_{max}$ ), and internal resistance of the device ( $R$ ) were measured by the Testing System for Thermoelectric cooling equipment (KA6288, China).

## 3 Results and discussion

### 3.1 Crystal structure and morphology of the $\text{Bi}_{(2-x)}\text{Sb}_x\text{Te}_3$ material

The crystal structures were fine-tuned by adjusting the stoichiometric ratios of the  $\text{Bi}_{(2-x)}\text{Sb}_x\text{Te}_3$  compounds. The XRD patterns of the as-prepared  $\text{Bi}_{(2-x)}\text{Sb}_x\text{Te}_3$  ( $x = 1.50\text{--}1.85$ ) samples (Fig. 1a) match well with the Bragg diffraction data of  $\text{Bi}_{0.5}\text{Sb}_{1.5}\text{Te}_3$  (JCPDS card No. 49-1713). No obvious impurity diffraction peak was observed in the XRD patterns. The three highest diffraction peaks are readily indexed to the (015), (1010), and (110) planes of the rhombohedral  $\text{Bi}_{0.5}\text{Sb}_{1.5}\text{Te}_3$  with space group of  $R\bar{3}m$  (No. 166). The diffraction intensity of (015) plane is far higher than that of the other diffraction peaks, which indicating that the samples have strong orientation characteristics. Fig. 1b is the enlarged XRD patterns of (015) peaks. With the Sb composition ( $x$ ) in  $\text{Bi}_{(2-x)}\text{Sb}_x\text{Te}_3$  compounds increasing from 1.50 to 1.85, the  $2\theta$  angles of the (015) peaks gradually shift from  $28.10^\circ$  to  $28.24^\circ$ , which indicate that a constriction on the lattice structure occurred. The lattice distortions resulting from the increasing of Sb element can be calculated according to the Bragg equation combining with the lattice formula of rhombohedral structure:

$$n\lambda = 2d_{hkl}\sin\theta \quad (1)$$

$$\frac{1}{d_{hkl}^2} = \frac{4(h^2 + hk + k^2)}{3a^2} + \frac{l^2}{c^2} \quad (2)$$

where  $n$  is an integer;  $\lambda$  is the wavelength of the diffraction wave (1.5406 Å);  $h$ ,  $k$ , and  $l$  are the indices of the crystallograph-

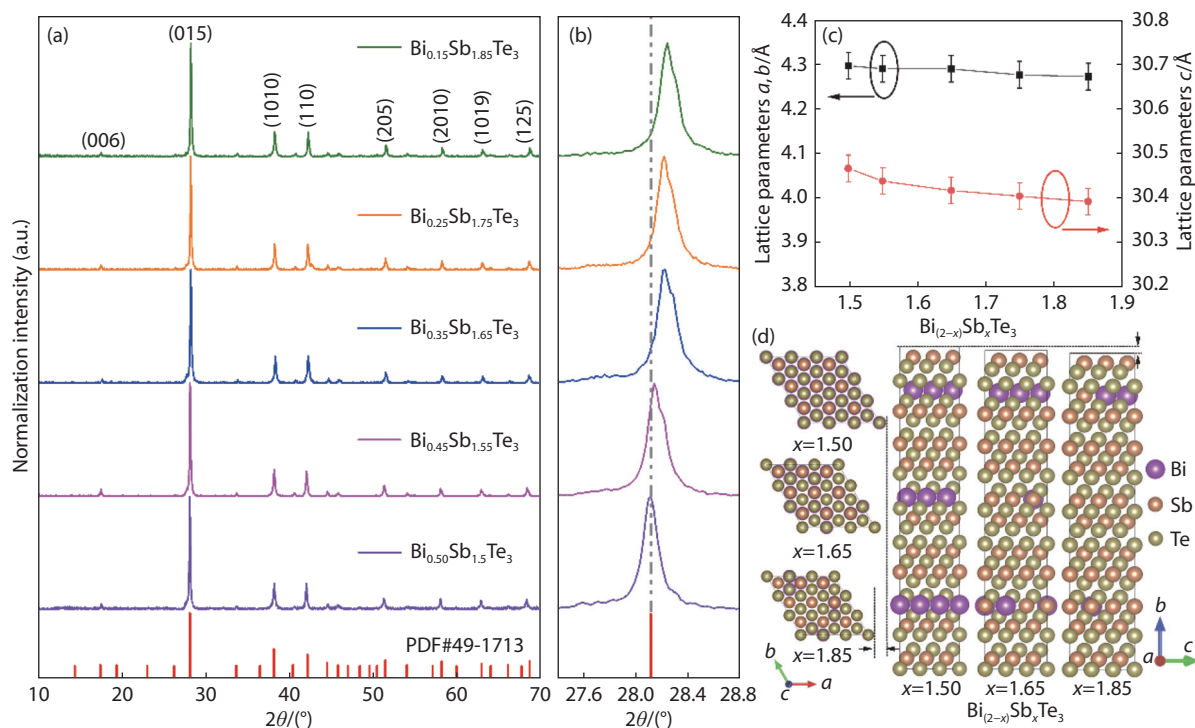


**Fig. 1** (a, b) XRD patterns, and partly enlarged figure, (c) lattice constants of  $\text{Bi}_{(2-x)}\text{Sb}_x\text{Te}_3$  composites with  $x$  were varied from 1.50 to 1.85. (d) Simulated structures of  $\text{Bi}_{0.5}\text{Sb}_{1.5}\text{Te}_3$ ,  $\text{Bi}_{0.35}\text{Sb}_{1.65}\text{Te}_3$ , and  $\text{Bi}_{0.15}\text{Sb}_{1.85}\text{Te}_3$  samples.

ic plane;  $d_{hkl}$  is the interplanar spacing. Lattice parameters  $a$ ,  $b$ , and  $c$  decreased as the Sb content was increased from  $x = 1.50$  to 1.85 owing to the different atomic radius sizes of Sb (141 pm) and Bi (182 pm). The linearly change of lattice parameters illustrates that the Sb atoms occupies Bi sites reasonably due to the same crystal structure between  $\text{Sb}_2\text{Te}_3$  and  $\text{Bi}_2\text{Te}_3$ , which also is consistent with previous reports<sup>[41]</sup>. The crystal structures of  $\text{Bi}_{(2-x)}\text{Sb}_x\text{Te}_3$  compounds with  $x = 1.50, 1.65, 1.85$  were simulated theoretically with multiple structural optimizations, in which a similar structure shrink is observed along the  $a$ - and  $c$ -axis directions (Fig. 1c).

In the previous literature, quintuple layer with a characteristic of ionic and covalent bonding was found in the rhombohedral  $\text{Bi}_{(2-x)}\text{Sb}_x\text{Te}_3$ <sup>[42]</sup>. The weak van der Waals interaction force exists between the layers, which resulting in a difficult growth along the out-plane direction. Experimentally, the stratified structures with thickness about 0.5  $\mu\text{m}$  were observed in the  $\text{Bi}_{(2-x)}\text{Sb}_x\text{Te}_3$  composites (Fig. 2a). Predictably, the low thickness and diameter of the  $\text{Bi}_{(2-x)}\text{Sb}_x\text{Te}_3$  layers, as well as the holes will enhance the confinement effect of the phonons with short and medium waves due to the increased amounts of lattice defects and grain boundaries<sup>[43]</sup>. More interestingly, the as-prepared  $\text{Bi}_{(2-x)}\text{Sb}_x\text{Te}_3$  composites is inhomogeneous crystal though there is no diffraction peak of the impure phase was observed in the XRD patterns. The elemental distribution mappings of  $\text{Bi}_{0.35}\text{Sb}_{1.65}\text{Te}_3$  sample (Fig. 2b–d) reveal that the Sb and Te elements are distributed evenly, however, some Bi-absent areas with a few microns were observed in the energy dispersive spectrometer (EDS) mapping. These results indicate that the some  $\text{Sb}_2\text{Te}_3$  compounds were precipitated from the  $\text{Bi}_{0.35}\text{Sb}_{1.65}\text{Te}_3$  bulks due to its limited solid solubility.

To further confirm the precipitation phenomenon of  $\text{Sb}_2\text{Te}_3$  compound, TEM observation was performed in the  $\text{Bi}_{0.35}\text{Sb}_{1.65}\text{Te}_3$  sample. Lots of irregular inclusions with sizes arranged from 20s nm to 200s nm were observed in the high angle annular dark field scanning transmission electron microscope (HAADF-STEM) image (Fig. 3a, denoted by the red wire). Simultaneously, elemental distribution mappings of Bi, Sb, and Te (Fig. 3c–e), which are similar to that of SEM were detected on the second phase (red frame in Fig. 3a). In contrast with the uniform Sb and Te distribution (Fig. 3d and e), an obvious Bi-poor region was observed in Fig. 3c, which again proved that the precipitates are  $\text{Sb}_2\text{Te}_3$  compounds. And the sizes of the  $\text{Sb}_2\text{Te}_3$  precipitates located in a wide range from ~20 nm to ~4.0  $\mu\text{m}$  according to the SEM and TEM images. A high-resolution transmission electron microscopy (HRTEM) was recorded around a small  $\text{Sb}_2\text{Te}_3$  precipitate. In the precipitate (Zone 1 in Fig. 3f), the interplanar spacings of the three adjacent directions were approximately 3.198 Å, 3.024 Å and 2.402 Å (Fig. 3g), which correspond well to the  $(\bar{1} \ 1 \ 5)$ ,  $(0 \ 1 \ 5)$  and  $(\bar{1} \ 0 \ 10)$  planes of the rhombohedral  $\text{Sb}_2\text{Te}_3$ . In the matrix (Zone 2 in Fig. 3f), the similar interplanar spacings, 3.274 Å, 3.165 Å, and 2.433 Å were obtained in Fig. 3h, which can be identified as the  $(\bar{1} \ 1 \ 5)$ ,  $(0 \ 1 \ 5)$  and  $(\bar{1} \ 0 \ 10)$  planes of rhombohedral  $\text{Bi}_{0.35}\text{Sb}_{1.65}\text{Te}_3$ , respectively. The parallelogram relationship among these planes (the center transmission spot and the nearest three diffraction spots) are also can be confirmed in the fast Fourier transformed (FFT) pattern under the crystallographic zone axis of  $[10 \ 5 \ \bar{1}]$  (inset of Fig. 3i). Theoretically, there is a high intersolubility between  $\text{Sb}_2\text{Te}_3$  and  $\text{Bi}_{0.35}\text{Sb}_{1.65}\text{Te}_3$  due to its same rhombohedral structure. However, lots of lattice dislocations were recorded in the HRTEM figure (Fig. 3j) because of the stress disorder de-



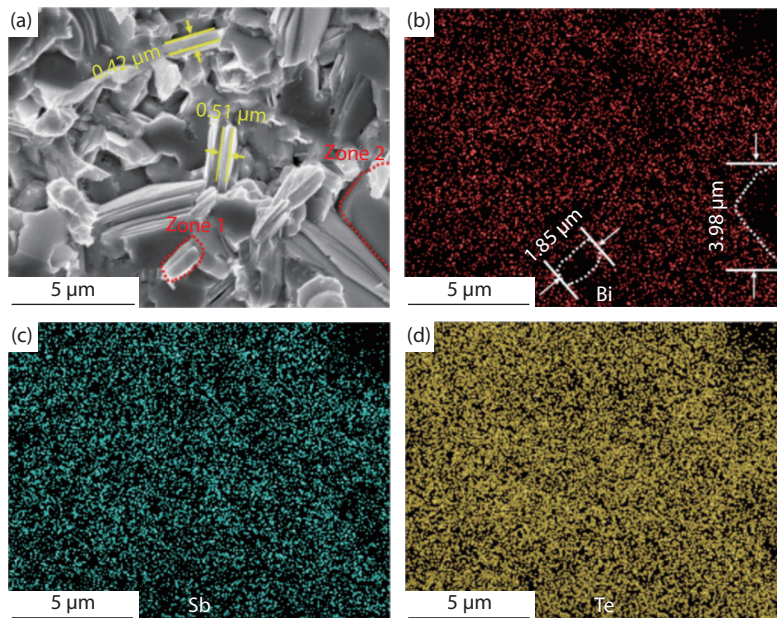


**Fig. 2** (a) Layer structures and grain sizes of the  $\text{Bi}_{0.35}\text{Sb}_{1.65}\text{Te}_3$  sample. (b–d) EDS mapping of Bi, Sb and Te elements on the fracture surface of  $\text{Bi}_{0.35}\text{Sb}_{1.65}\text{Te}_3$  sample.

living from the continuously increasing of Sb atoms. In addition, Fig. 3k presents the particle size distribution of the  $\text{Bi}_{0.35}\text{Sb}_{1.65}\text{Te}_3$  sample. Lots of nanoparticles with average diameters about 420 nm (inset of Fig. 3k) were observed. The results indicated that the microparticles that were detected in the SEM are made up of nanoparticles. Correspondingly, high density network of grain boundaries were found in the bulks prepared by mechanical alloying combining with SPS, which consistent with previous report<sup>[44]</sup>.

### 3.2 Electrical property of the $\text{Bi}_{(2-x)}\text{Sb}_x\text{Te}_3$ material

Generally, the antisite defects, point defects, and precipitates resulting from the ratio regulation have great contributions to adjust the electrical properties. With the temperature increasing, the electrical conductivities ( $\sigma$ ) of the  $\text{Bi}_{(2-x)}\text{Sb}_x\text{Te}_3$  samples decrease (Fig. 4a). Different from the intrinsic competition between Hall carrier concentrations ( $n_H$ ) and mobilities ( $\mu_H$ ) on most semiconductor materials, the synchronous enhancements were recorded on both  $n_H$  and  $\mu_H$  as Sb increasing. Specifically, the  $n_H$  (Fig. 4b) enhances from  $\sim 1.9 \times 10^{19} \text{ cm}^{-3}$  to  $\sim 3.9 \times 10^{19} \text{ cm}^{-3}$  when the proportion ( $x$ ) of Sb increases from 1.50 to 1.85. Probably, the increasing antisite defects ( $\text{Sb}_{\text{Te}}$ ) is the dominate reason for the increase of  $n_H$ , which can be defined as:

$$5Sb_{2\text{Te}_3} = 8Sb_{\text{Sb}}^x + 10Te_{\text{Te}}^x + 5Te_{(\text{g})} + (2V_{\text{Sb}}''' + 3V_{\text{Te}}'') + 2Sb_{\text{Te}}' + 2h^{\bullet} \quad (3)$$

Where  $V_{\text{Sb}}$ ,  $V_{\text{Te}}$  are Sb, Te vacancies,  $h$  is the produced hole, which can cause a increase of carrier concentration. Theoretically, Sb atom (141 pm) has a similar radius size to Te atom (137 pm), while the radius of Bi atom (182 pm) is much bigger than that of Te atom, which lead to the antisite defects formation energy of  $\text{Sb}_{\text{Te}}$  is more lower than that of  $\text{Bi}_{\text{Te}}$ , i.e.,  $E_{\text{AS}}(\text{Sb-Te}) < E_{\text{AS}}(\text{Bi-Te})$ , and means that the occupying phenomenon between Sb and Te atoms happened more easily as the Sb proportion increasing. At the same time, the alloy scattering that originated from the high concentration

of Bi atom in  $\text{Bi}_{0.5}\text{Sb}_{1.5}\text{Te}_3$  sample was gradually reduced along with the Bi proportion decreasing to  $\text{Bi}_{0.15}\text{Sb}_{1.85}\text{Te}_3$ . In this process, the lattice structures that had been destroyed by the Bi atoms were renovated as the Sb proportion increasing (i. e., Bi proportion decreasing). As a consequence, the carrier mobility of  $\text{Bi}_{(2-x)}\text{Sb}_x\text{Te}_3$  samples are enhanced from  $185 \text{ cm}^2\text{V}^{-1} \text{ s}^{-1}$  to  $300 \text{ cm}^2\text{V}^{-1} \text{ s}^{-1}$  monotonically with the Sb proportion ( $x$ ) increasing from 1.50 to 1.85.

The  $S$  decreases significantly from  $269 \mu\text{VK}^{-1}$  to  $124 \mu\text{VK}^{-1}$  (298 K) as the  $x$  increasing from 1.50 to 1.85 (Fig. 4d). Comparing with the  $\text{Bi}_{0.5}\text{Sb}_{1.5}\text{Te}_3$  sample with sharply reduced  $S$ , relatively flat  $S$  values were obtained in the  $\text{Bi}_{(2-x)}\text{Sb}_x\text{Te}_3$  samples with  $x \geq 1.55$ . Typically, the samples of  $x = 1.55$  and 1.65 exhibit high  $S$  values of  $\sim 200 \mu\text{VK}^{-1}$  throughout the whole temperature range (298–498 K, Fig. 4d). More importantly, the  $S_{\text{max}}$  peaks gradually shift to the high temperatures when the Sb proportion was increased, which probably because the degeneracies of the samples are enhanced, and the intrinsic semiconductive conduction were inhibited by the increased hole concentrations. The carrier effective mass  $m^*$  of  $(\text{Bi}_{(2-x)}\text{Sb}_x\text{Te}_3)$  samples can be calculated using the degenerate formula:

$$S = \frac{8\pi^2 k_B^2}{3eh^2} m^* T \left( \frac{\pi}{3n} \right)^{2/3} \quad (4)$$

where  $k_B$  and  $h$  are Boltzmann constant and Planck constant, separately. The  $m^*$  values gradually reduce from  $0.88 m_e$  to  $0.67 m_e$  with the  $x$  increasing from 1.50 to 1.85. On account of these  $m^*$  values, and also assume the carrier scattering is acoustic scattering ( $\lambda = 0$ ), the  $S$  and  $n$  can be described using the following formulas based on the single parabolic band model:

$$n = 4\pi \left( \frac{2m^* k_B T}{h^2} \right) F_{\lambda}(\eta) \quad (5)$$

$$S = \frac{k_B}{e} \left[ \frac{(\lambda + 2)F_{\lambda+1}(\eta)}{(\lambda + 1)F_{\lambda}(\eta)} - \eta \right] \quad (6)$$

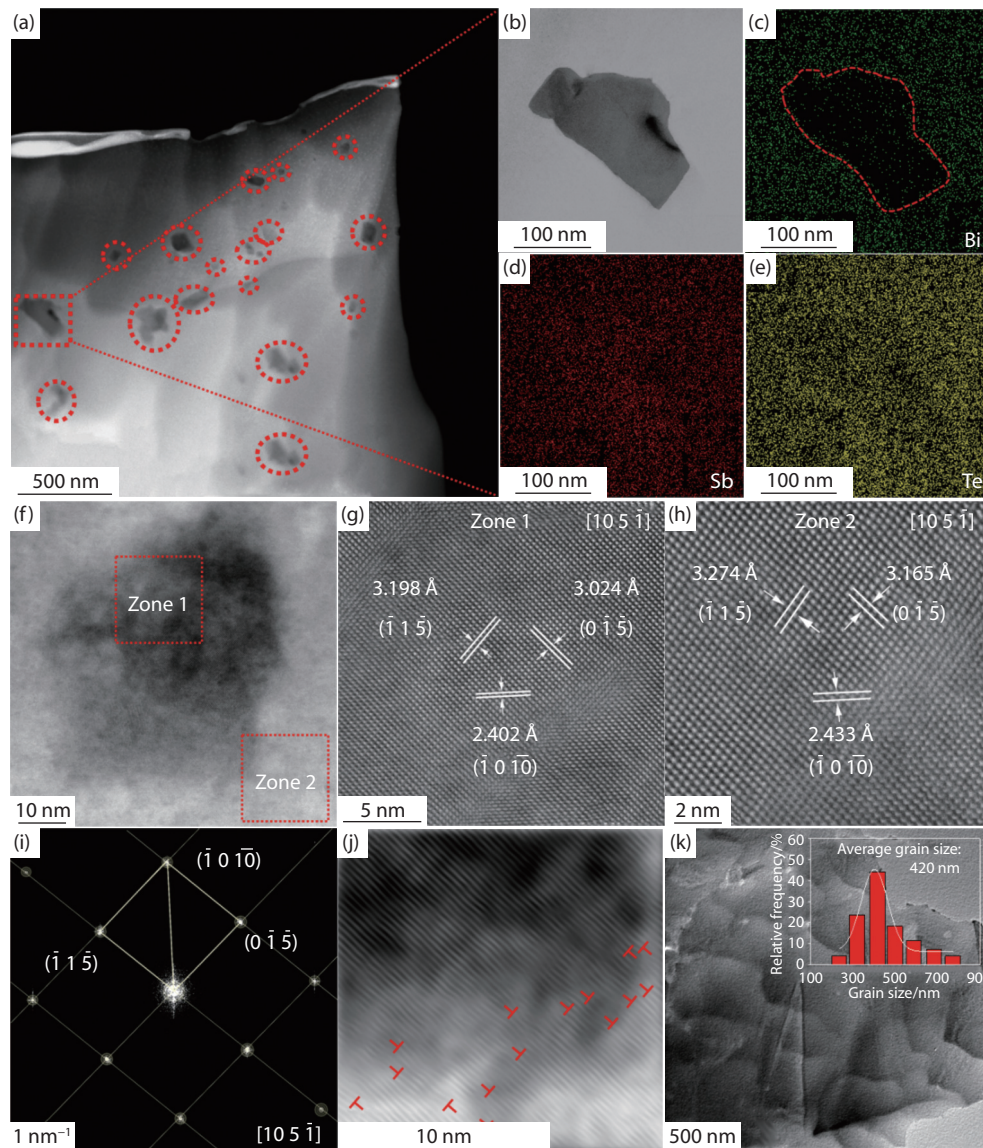


**Fig. 3** (a, b) HAADF-STEM images of  $\text{Bi}_{0.35}\text{Sb}_{1.65}\text{Te}_3$  sample. (c–e) EDX mapping patterns of Bi, Sb, and Te elements around the precipitate in a  $\text{Bi}_{0.35}\text{Sb}_{1.65}\text{Te}_3$  crystal. (f) TEM image of  $\text{Bi}_{0.35}\text{Sb}_{1.65}\text{Te}_3$ -based compound. (g, h) HRTEM images of  $\text{Sb}_2\text{Te}_3$  precipitate (Zone 1 in (f)) and  $\text{Bi}_{0.35}\text{Sb}_{1.65}\text{Te}_3$  matrix (Zone 2 in (f)), respectively. (i, j) FFT and lattice dislocation images of  $\text{Bi}_{0.35}\text{Sb}_{1.65}\text{Te}_3$  matrix. (k) Morphology and size distribution of  $\text{Bi}_{0.35}\text{Sb}_{1.65}\text{Te}_3$  nanoparticles.

$$F_{\lambda}(\eta) = \int_0^{\infty} \frac{x^{\lambda} dx}{1 + \exp(x - \eta)} \quad (7)$$

Where  $F_{\lambda}(\eta)$  is Fermi integral,  $\eta$  is reduced Fermi level,  $\eta = E_f/k_B T$ . The Pisarenko relation between  $S$  and  $n_H$  are shown as the solid lines in Fig. 4e. In summary, the experimental  $S$  values locate above the calculate values, which indicate that the ionized impurity scattering ( $\lambda = 2$ ) derived from the antisite defects, the neutral impurity scattering ( $\lambda = 0.5$ ) originated from the  $\text{Sb}_2\text{Te}_3$  precipitates, in addition to acoustic scattering and alloy scattering ( $\lambda = 0$ ), also give some contribution to increase the total  $\lambda$  and  $S$ . Consequently, the  $PF$  are gradually increased from  $2.1 \times 10^{-3} - 0.6 \times 10^{-3} \text{ Wm}^{-1} \text{ K}^{-2}$  (298–498 K,  $\text{Bi}_{0.5}\text{Sb}_{1.5}\text{Te}_3$ ) to  $4.3 \times 10^{-3} - 2.6 \times 10^{-3} \text{ Wm}^{-1} \text{ K}^{-2}$  (298–498 K,  $\text{Bi}_{0.25}\text{Sb}_{1.75}\text{Te}_3$ ) as Fig. 4f has shown. The maximum  $PF \sim 4.3 \times 10^{-3} \text{ Wm}^{-1} \text{ K}^{-2}$  are over 2.1 times of that of  $\text{Bi}_{0.5}\text{Sb}_{1.5}\text{Te}_3$  sample at room temperature (Fig. 4f).

### 3.3 Thermal performance and $zT$ value of the $\text{Bi}_{(2-x)}\text{Sb}_x\text{Te}_3$ material

The total thermal conductivities ( $\kappa_{tot}$ ) of  $\text{Bi}_{(2-x)}\text{Sb}_x\text{Te}_3$  samples show a wide dispersion (Fig. 5a) at room temperature, which are monotonically increased from  $0.83 \text{ Wm}^{-1} \text{ K}^{-1}$  ( $\text{Bi}_{0.5}\text{Sb}_{1.5}\text{Te}_3$ ) to  $1.92 \text{ Wm}^{-1} \text{ K}^{-1}$  ( $\text{Bi}_{0.15}\text{Sb}_{1.85}\text{Te}_3$ ). On the contrary, relatively agminated points ( $1.22 - 1.44 \text{ Wm}^{-1} \text{ K}^{-1}$ ) of  $\kappa_{tot}$  are observed at the high temperature (498 K). Thus, the slope factors of the  $\kappa_{tot}$  are reduced sharply with the  $x$  of  $\text{Bi}_{(2-x)}\text{Sb}_x\text{Te}_3$  increasing from 1.50 to 1.85, which probably associate with the gradually delayed intrinsic excitation. The  $\kappa_{tot}$  is the sum of the electron thermal conductivity ( $\kappa_e$ ), the lattice thermal conductivity ( $\kappa_l$ ), and the bipolar thermal conductivity ( $\kappa_{bip}$ ), i. e.  $\kappa_{tot} = \kappa_e + \kappa_l + \kappa_{bip}$ .  $\kappa_e$  can be estimated using the Wiedemann-Franz law,  $\kappa_e = \sigma LT$ , in which  $L$  is the Lorenz constants of the degenerate semiconductors that can be estimated using



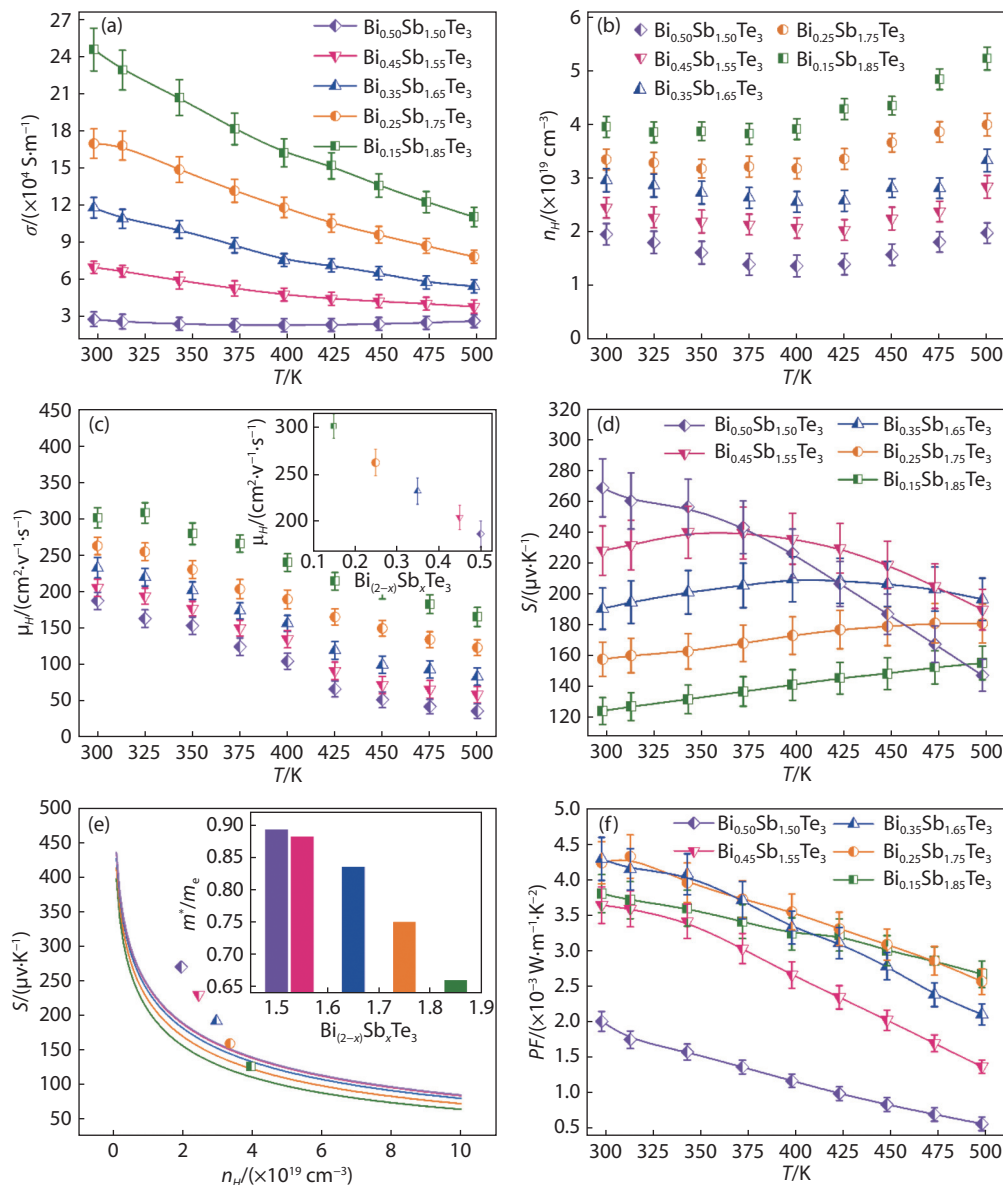


**Fig. 4** (a) Electrical conductivities, (b) Hall carrier concentrations, (c) Hall carrier mobilities, (d) Seebeck coefficients, (e) Pisarenko plots and effective mass, (f) power factors of the  $\text{Bi}_{(2-x)}\text{Sb}_x\text{Te}_3$  samples.

$L \approx 1.5 + \exp\left(-\frac{|S|}{116}\right)$ . Thus, the tendency of  $L$  (Fig. 5b) and  $\kappa_e$  (Fig. 5c) curves are conformed to the  $S$  and  $\sigma$  values, respectively. The  $\kappa_e$  at 298 K increase from  $0.13 \text{ Wm}^{-1} \text{ K}^{-1}$  to  $1.35 \text{ Wm}^{-1} \text{ K}^{-1}$  with the  $x$  of  $\text{Bi}_{(2-x)}\text{Sb}_x\text{Te}_3$  increasing from 1.50 to 1.85 (Fig. 5c). The sum of the  $\kappa_l$  and  $\kappa_{bip}$  can be obtained by deducting the  $\kappa_e$  from  $\kappa_{tot}$  (Fig. 5d). With the test temperature increasing, all the  $\kappa_l + \kappa_{bip}$  curves show an upward trend, which resulting from the bipolar effect. Theoretically, the high  $n_H$  can inhibit the intrinsic thermal excitation, and delay the bipolar effect to high temperature. Thus, the more Sb added, the higher temperature of the inflection point of bipolar diffusion effect was put off (Fig. 5d). Moreover, the  $\kappa_l$  of all samples decrease with the Sb contents increasing. We assume that the increase amount of  $\text{Sb}_2\text{Te}_3$  nano-precipitates, and  $\text{Sb}_{\text{Te}}$  antisite defects enhance the multifrequency phonon scattering.

Typically,  $\kappa_l$  of the  $\text{Bi}_{0.15}\text{Sb}_{1.85}\text{Te}_3$  sample (at 423 K) is 64% lower than that of  $\text{Bi}_{0.5}\text{Sb}_{1.5}\text{Te}_3$  sample. Fig. 5e shows the possible mechanisms of the multifrequency phonon scattering in the as-obtained samples. The increased point defects, pores,  $\text{Sb}_2\text{Te}_3$  nano-precipitates, as well as the deuterogenic grain boundaries and dislocations are impede the transport of phonons with short, middle and long wavelengths, and resulting in a low value of  $\kappa_l$ .

Fig. 6 shows the temperature dependence of the peak  $zT$  ( $zT_{max}$ ) and average  $zT$  ( $zT_{avg}$ ) values of the  $\text{Bi}_{(2-x)}\text{Sb}_x\text{Te}_3$  samples and the state-of-the-art P-type  $\text{Bi}_{(2-x)}\text{Sb}_x\text{Te}_3$ -based materials. In summary, the  $n_H$  can be optimized by adjusting the element ratios and anti-site defects. As our studies show, medium  $n_H$  values in favor of relatively high  $PF$ , and also beneficial to delay the bipolar diffusion effect. The  $PF$  of  $\text{Bi}_{0.35}\text{Sb}_{1.65}\text{Te}_3$  and  $\text{Bi}_{0.25}\text{Sb}_{1.75}\text{Te}_3$  samples as high as

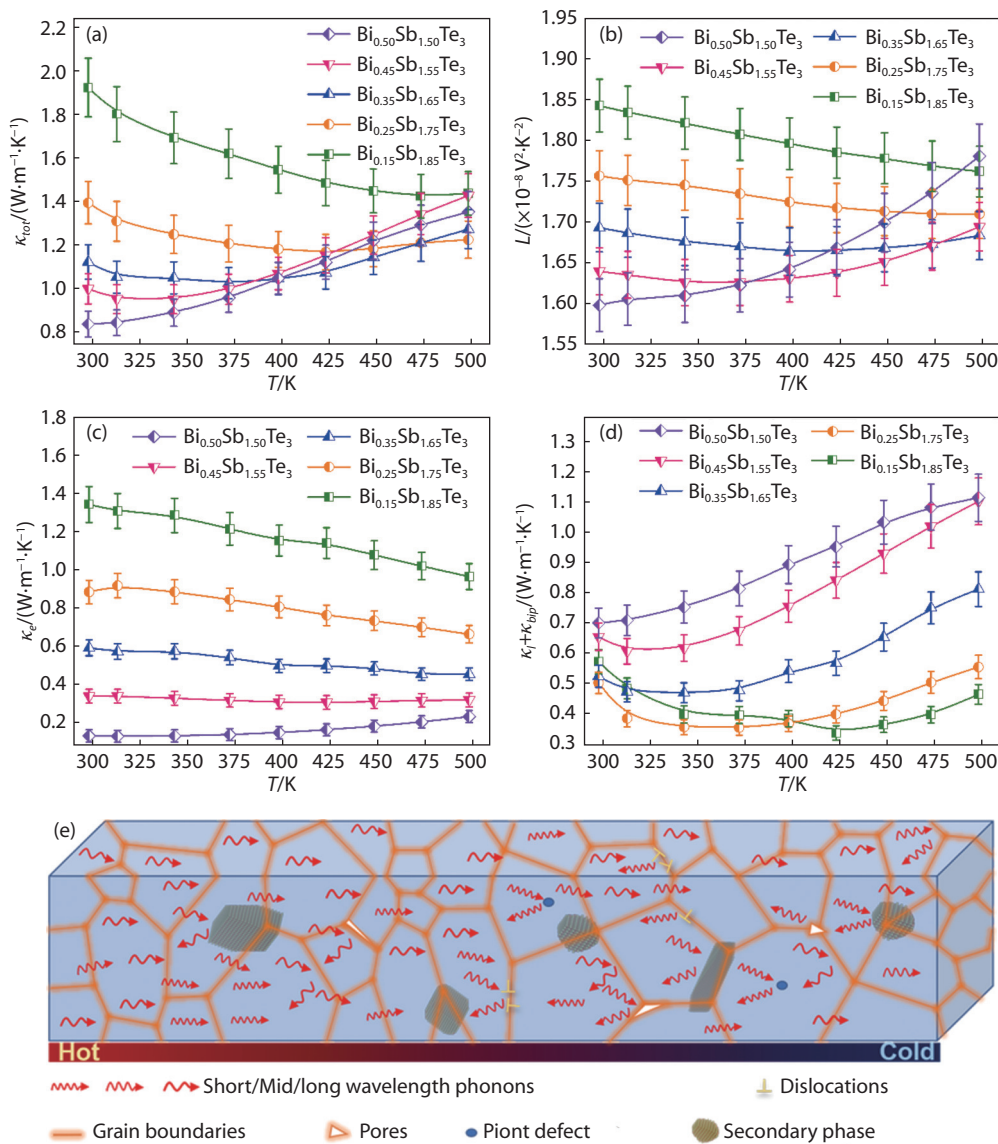


**Fig. 5** (a–d) Temperature-dependent  $\kappa_{tot}$ ,  $L$ ,  $\kappa_e$ ,  $\kappa_l + \kappa_{lpp}$  and  $zT$  values of the as-obtained samples with  $x$  increased from 1.50 to 1.85. (e) The possible scattering mechanism of phonons with different wavelengths in the Bi<sub>(2-x)</sub>Sb<sub>x</sub>Te<sub>3</sub> sample.

$4.3 \pm 0.1 \times 10^{-3} \text{ Wm}^{-1} \text{ K}^{-2}$  at room temperature. Correspondingly, the deferred bipolar diffusion effect also results in low  $\kappa_{tot}$  values over the entire working temperature range. As the result, relatively high  $zT_{max}$  value  $\sim 1.35$  at 373 K was obtained in the Bi<sub>0.35</sub>Sb<sub>1.65</sub>Te<sub>3</sub> sample, and the  $zT$  values change mildly throughout the test temperature interval (Fig. 6a). The  $zT_{max}$  of Bi<sub>0.35</sub>Sb<sub>1.65</sub>Te<sub>3</sub> sample is  $\sim 47\%$  higher than that of Bi<sub>0.5</sub>Sb<sub>1.5</sub>Te<sub>3</sub> sample, and also a little higher than that of the state-of-the-art P-type Bi<sub>(2-x)</sub>Sb<sub>x</sub>Te<sub>3</sub>-based materials, whose  $zT_{max}$  values are about 0.95 (commercial ingot)<sup>[45]</sup>, 1.16<sup>[38]</sup>, 1.18<sup>[29]</sup> (Fig. 6b). Among all the Bi<sub>(2-x)</sub>Sb<sub>x</sub>Te<sub>3</sub> samples, a highest  $zT_{avg}$  as high as 1.18, was obtained in the Bi<sub>0.35</sub>Sb<sub>1.65</sub>Te<sub>3</sub>, which is 162% higher than that of Bi<sub>0.5</sub>Sb<sub>1.5</sub>Te<sub>3</sub> sample ( $zT_{avg}$  0.45), as well as higher than the commercial ingot 0.76 ( $zT_{max} = 0.95$ )<sup>[45]</sup>, and most state-of-the-art studies 0.86 ( $zT_{max} = 1.18$ )<sup>[29]</sup>, 0.9 ( $zT_{max} = 1.16$ )<sup>[38]</sup>, 0.96 ( $zT_{max} = 1.38$ )<sup>[20]</sup>, 1.09 ( $zT_{max} = 1.4$ )<sup>[14]</sup>, 1.14 ( $zT_{max} = 1.5$ )<sup>[46]</sup>, which is conducive to the im-

provement of the TE conversion efficiency of the device.

### 3.4 Thermoelectric performance of the Bi<sub>(2-x)</sub>Sb<sub>x</sub>Te<sub>3</sub>-based device

TE devices with 127 pairs couples were assembled using our P-type Bi<sub>(2-x)</sub>Sb<sub>x</sub>Te<sub>3</sub>-based materials and commercial N-type Bi(Te,Se) ingots with  $PF_{max}$  about  $2.68 \times 10^{-3} \text{ Wm}^{-1} \text{ K}^{-2}$ , and  $zT_{max}$  value  $\sim 0.93$  at room temperature. The simulated construction was shown in Fig. 7a, including the ceramic substrates, electrical interconnect, P/N-type semiconductor and wires. The maximum temperature difference ( $\Delta T_{max}$ ) between the two ends of junction can be calculated by the following equation:

$$\Delta T = \frac{S_{np}T_c - \frac{1}{2}I^2R - Q_c}{\kappa} \quad (8)$$

Where  $S_{np}$  is the sum of absolute value Seebeck coefficients of the N- and P-type materials.  $T_c$  is the temperature of

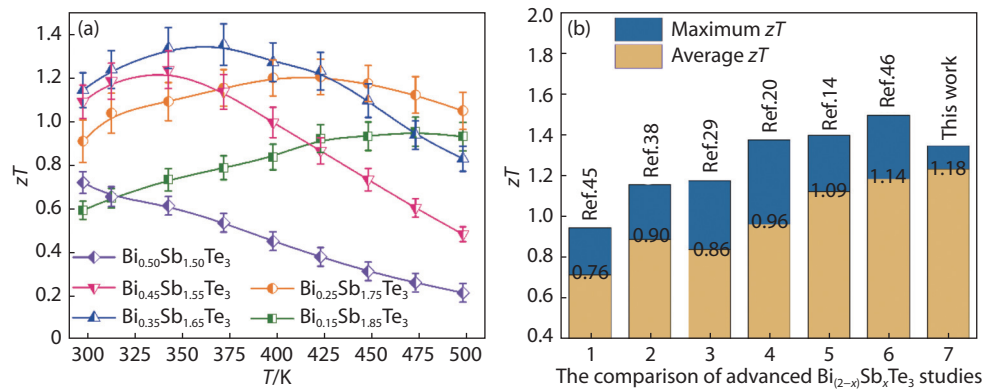


**Fig. 6** (a) Temperature-dependent  $zT$  values of the  $\text{Bi}_{(2-x)}\text{Sb}_x\text{Te}_3$  samples with different element ratios. (b) A comparison of  $zT_{\max}$  and  $zT_{\text{avg}}$  values between our sample and the state-of-the-art P-type  $\text{Bi}_{(2-x)}\text{Sb}_x\text{Te}_3$ -based materials.

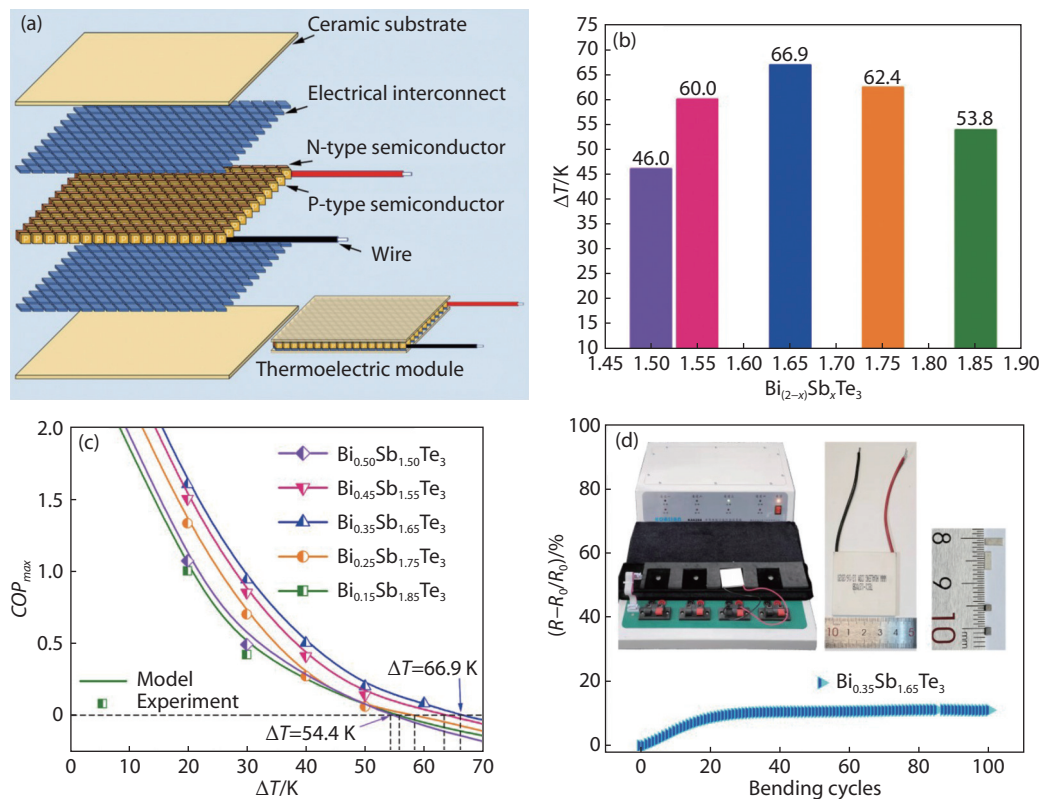


**Fig. 7** (a) Simulated construction of the thermoelectric device. (b) The maximum  $\Delta T$  values of the  $\text{Bi}_{(2-x)}\text{Sb}_x\text{Te}_3$ -based devices. (c) The maximum  $COP$  values of the  $\text{Bi}_{(2-x)}\text{Sb}_x\text{Te}_3$ -based devices as a function of the maximum  $\Delta T$ . (d) The dependence of relative resistance of the  $\text{Bi}_{0.35}\text{Sb}_{1.65}\text{Te}_3$ -based devices. Insets of (d) are the detailed sizes of P/N legs, device, and information of the test equipment.

the cold junction.  $I$  is the current injected into the device, and  $R$  is the internal resistance of the device.  $Q_C$  is thermal loads applied on the cold junction.  $k$  is total thermal conductance of N- and P-type legs. Fig. 7b shows that the  $\Delta T_{\max}$  tested at room temperature basically obey the objective law of the  $zT$  values of  $\text{Bi}_{(2-x)}\text{Sb}_x\text{Te}_3$  samples. The  $\Delta T_{\max}$  of the  $\text{Bi}_{0.35}\text{Sb}_{1.65}\text{Te}_3$  and  $\text{Bi}_{0.25}\text{Sb}_{1.75}\text{Te}_3$ -based devices are as high as 66.9 K ( $zT = 1.14$  at RT) and 62.4 K ( $zT = 0.91$  at RT), which are about 45% and 36% higher than that of  $\text{Bi}_{0.50}\text{Sb}_{1.50}\text{Te}_3$  ( $zT = 0.72$  at RT,  $\Delta T_{\max} \sim 46$  K) sample, and these values also higher than the latest researches on  $\text{Bi}_{(2-x)}\text{Sb}_x\text{Te}_3$ -based devices with  $\Delta T_{\max} \sim 43$  K<sup>[47]</sup>, 55 K<sup>[48]</sup>, and 60 K<sup>[49]</sup>.

The maximum coefficient of performance ( $COP_{\max}$ ) can be calculated using the following equation<sup>[50]</sup>:

$$COP_{\max} = \frac{T_c}{T_h - T_c} \times \frac{\sqrt{1 + z \frac{(T_h - T_c)}{2}} - \frac{T_h}{T_c}}{\sqrt{1 + z \frac{(T_h - T_c)}{2}} + 1} \quad (9)$$

$COP$  is the cooling capacity divided by the electrical energy that was input to the device. Based on the test  $z$  and  $\Delta T$  values, the  $COP_{\max}$  of the  $\text{Bi}_{(2-x)}\text{Sb}_x\text{Te}_3$ -based devices were calculated and listed in Fig. 7c. The intercept on the function of  $COP_{\max}$  and  $\Delta T$  represent the maximum  $\Delta T$  values that the devices can reached under the optimal current. A distinct



competitive relationship between  $\Delta T$  and  $COP_{max}$  values was observed in the curves, which resulting in the high  $COP_{max}$  values were obtained at low  $\Delta T$ . A width  $COP_{max}$  range from 0.9 ( $Bi_{0.15}Sb_{1.85}Te_3$ ) to 1.7 ( $Bi_{0.35}Sb_{1.65}Te_3$ ) was found with the  $\Delta T$  is about 20 K, and a narrow  $COP_{max}$  scope from 0.10 ( $Bi_{0.15}Sb_{1.85}Te_3$ ) to 0.24 ( $Bi_{0.35}Sb_{1.65}Te_3$ ) was obtained with the  $\Delta T$  is about 50 K. Thus, the  $zT$  values has a great contribution to enhance the  $COP_{max}$  values particularly at low  $\Delta T$ . Time effect property of semiconductor is crucial for the Peltier cooler also. To test the stability of the devices, the assembled Peltier coolers were charged by a forward and reverse currents for about 100 times. Typically, a process cycle includes 6 seconds 12 V direct current, 18 seconds stopping, 6 seconds 12 V reverse current, and 0.5 h free cooling. As shown in Fig. 7d, the relative resistance of the Peltier cooler initially increase  $\sim 12.0\%$ , and then tend to be a constant after passing direct current 40 cycles, which indicates that the Peltier cooler possess a relatively stable performance.

## 4 Conclusions

In summary,  $Bi_{(2-x)}Sb_xTe_3$ -based composites samples with excellent TE properties were prepared by mechanical alloying combined with SPS. By adjusting the ratio of Bi:Sb, the hole concentration was enhanced from  $1.9 \times 10^{19} \text{ cm}^{-3}$  to  $3.9 \times 10^{19} \text{ cm}^{-3}$  along with the increasing amount of antisite defects. Consequently, the peak  $PF$  of  $4.3 \times 10^{-3} \text{ Wm}^{-1} \text{ K}^{-2}$  was achieved in the  $Bi_{0.35}Sb_{1.65}Te_3$  sample. The  $\kappa_{tot}$  values were heavily suppressed via delaying the bipolar effect, as well as increasing the scattering of low and middle frequency phonons by  $Sb_2Te_3$  second phases. A remarkable  $zT$  value of about 1.35 at 373 K was obtained in the  $Bi_{0.35}Sb_{1.65}Te_3$  sample. A high average  $zT$  value of 1.18 was obtained in the  $Bi_{0.35}Sb_{1.65}Te_3$  sample over a wide working temperature range (from 298 to 498 K). The Peltier cooler devices assembled with  $Bi_{(2-x)}Sb_xTe_3$ -based materials and commercial N-type  $Bi(Te,Se)$  ingots show the  $\Delta T_{max}$  as high as 66.9 K. The relatively high  $COP_{max}$  and stable performance of the as-obtained devices were also proved. Predictably, much higher TE performance can be obtained via a further energy band engineering, nanoengineering and texture controlling depending on the currently optimized element proportion. The simple preparation technology, optimization strategy of the performance and the high TE properties will give some guiding significance for the preparation of other TE properties and devices.

## Acknowledgements

This work was supported by the S&T Program of Hebei (No. 206Z4403G), Outstanding Youth Science Fund Project of Natural Science Foundation of Hebei Province (No. A2020201032), National Natural Science Foundation of China (No. 51972094), and Innovation Team Project of Hebei University (No. 150000321008). This work was supported in part by the Microanalysis Center and the High-Performance Computing Center of Hebei University.

## Conflict of interest

The authors declare no conflict of interest.

## Author contributions

The manuscript was drafted by Xiaofeng Yang, Qing Wang and revised by Prof. Zhiliang Li and Shufang Wang. All authors had approved the final version of the manuscript.

## REFERENCES

1. L. E. Bell, *Science*, 2008, 321, 1457
2. A. F. Ioffe, L. S. Stil'bans, E. K. Iordanishvili, T. S. Stavitskaya and A. G. Vineyard, *Phys. Today*, 1959, 12, 42
3. X. Lu, P. Jiang, X. Bao, *Nat. Commun.*, 2019, 10, 1
4. G. J. Snyder, E. S. Toberer, *Nat. Mater.*, 2008, 7, 105
5. Y. Pei, X. Shi, A. LaLonde, H. Wang, L. Chen, G. J. Snyder, *Nature*, 2011, 473, 66
6. F. J. Disalvo, *Science*, 1999, 285, 703
7. J. P. Heremans, V. Jovovic, E. S. Toberer, A. Saramat, K. Kurosaki, A. Charoenphakdee, S. Yamanaka, G. J. Snyder, *Science*, 2008, 321, 554
8. B. Poudel, Q. Hao, Y. Ma, Y. Lan, A. Minnich, B. Yu, X. Yan, D. Wang, A. Muto, D. Vashaee, X. Chen, J. Liu, M. S. Dresselhaus, G. Chen, Z. Ren, *Science*, 2008, 320, 634
9. X. Zhang, D. Wang, H. Wu, M. Yin, Y. Pei, S. Gong, L. Huang, S. J. Pennycook, J. He, L.-D. Zhao, *Energy Environ. Sci.*, 2017, 10, 2420
10. Q. Zhang, Q. Zhang, S. Chen, W. Liu, K. Lukas, X. Yan, H. Wang, D. Wang, C. Opeil, G. Chen, Z. Feng, *Nano Energy*, 2012, 1, 183
11. X. Chen, L. Liu, Y. Dong, L. Wang, L. Chen, W. Jiang, *Prog. Nat. Sci-mater.*, 2012, 22, 201
12. L. Hu, T. Zhu, X. Liu, X. Zhao, *Adv. Funct. Mater.*, 2014, 24, 5211
13. T. Zhu, Z. Xu, J. He, J. Shen, S. Zhu, L. Hu, T. M. Tritt, X. Zhao, *J. Mater. Chem. A*, 2013, 1, 11589
14. J.-J. Shen, T.-J. Zhu, X.-B. Zhao, S.-N. Zhang, S.-H. Yang, Z.-Z. Yin, *Energy Environ. Sci.*, 2010, 3, 1519
15. L.-P. Hu, T.-J. Zhu, Y.-G. Wang, H.-H. Xie, Z.-J. Xu, X.-B. Zhao, *Npg Asia Mater.*, 2014, 6, e88
16. Z. J. Xu, L. P. Hu, P. J. Ying, X. B. Zhao, T. J. Zhu, *Acta Mater.*, 2015, 84, 385
17. J. Jiang, L.-D. Chen, S. Bai, Q. Yao, Q. Wang, *Scripta Mater.*, 2005, 52, 347
18. R. Deng, X. Su, Z. Zheng, L. Wei, Y. Yan, Q. Zhang, V. P. Dravid, C. Uher, M. G. Kanatzidis, X. Tang, *Sci. Adv.*, 2018, 4, eaar5606
19. Y. Pan, U. Aydemir, J. A. Grovogui, I. T. Witting, R. Hanus, Y. Xu, J. Wu, C.-F. Wu, F.-H. Sun, H.-L. Zhuang, J.-F. Dong, J.-F. Li, V. P. Dravid, G. J. Snyder, *Adv. Mater.*, 2018, 30, 1802016
20. Y. Pan, Y. Qiu, I. Witting, L. Zhang, C. Fu, J.-W. Li, Y. Huang, F.-H. Sun, J. He, G. J. Snyder, C. Felser, J.-F. Li, *Energy Environ. Sci.*, 2019, 12, 624
21. H.-L. Zhuang, J. Pei, B. Cai, J. Dong, H. Hu, F.-H. Sun, Y. Pan, G. J. Snyder, J.-F. Li, *Adv. Funct. Mater.*, 2021, 31, 2009681
22. Y. Q. Cao, T. J. Zhu, X. B. Zhao, X. B. Zhang, J. P. Tu, *Appl. Phys. A*, 2008, 92, 321
23. Y. Q. Cao, X. B. Zhao, T. J. Zhu, X. B. Zhang, J. P. Tu, *Appl. Phys. Lett.*, 2008, 92, 143106
24. S. Cao, Z.-Y. Huang, F.-Q. Zu, J. Xu, L. Yang, Z.-G. Chen, *Acs Appl. Mater. Inter.*, 2017, 9, 36478
25. Z.-Y. Huang, H. Zhang, L. Yang, B. Zhu, K. Zheng, M. Hong, Y. Yu, F.-Q. Zu, J. Zou, Z.-G. Chen, *Mater. Today Energy*, 2018, 9, 383
26. Y. Zheng, H. Xie, Q. Zhang, A. Suwardi, X. Cheng, Y. Zhang, W. Shu, X. Wan, Z. Yang, Z. Liu, X. Tang, *Acs Appl. Mater. Inter.*, 2020, 12, 36186

27. W. Xie, J. He, H. J. Kang, X. Tang, S. Zhu, M. Laver, S. Wang, J. R. D. Copley, C. M. Brown, Q. Zhang, T. M. Tritt, *Nano Lett.*, 2010, 10, 3283
28. J. Qiu, Y. Yan, H. Xie, T. Luo, F. Xia, L. Yao, M. Zhang, T. Zhu, G. Tan, X. Su, J. Wu, C. Uher, H. Jiang, X. Tang, *Sci. China Mater.*, 2021, 64, 1507
29. G. Zheng, X. Su, H. Xie, Y. Shu, T. Liang, X. She, W. Liu, Y. Yan, Q. Zhang, C. Uher, M. G. Kanatzidis, X. Tang, *Energy Environ. Sci.*, 2017, 10, 2638
30. H. Huang, J. Li, S. Chen, Z. Zhang, Y. Yan, X. Su, X. Tang, *J. Solid State Chem.*, 2020, 288, 121433
31. J.-Z. Xin, C.-G. Fu, W.-J. Shi, G.-W. Li, G. Auffermann, Y.-P. Qi, T.-J. Zhu, X.-B. Zhao, C. Felser, *Rare Metals*, 2018, 37, 274
32. Q. Zhang, R. Zhai, T. Fang, K. Xia, Y. Wu, F. Liu, X. Zhao, T. Zhu, *J. Alloys Compd.*, 2020, 831, 154732
33. F. Hao, P. Qiu, Y. Tang, S. Bai, T. Xing, H.-S. Chu, Q. Zhang, P. Lu, T. Zhang, D. Ren, J. Chen, X. Shi, L. Chen, *Energy Environ. Sci.*, 2016, 9, 3120
34. M. Tan, W.-D. Liu, X.-L. Shi, J. Shang, H. Li, X. B. Liu, L. Z. Kou, M. Dargusch, Y. Deng, Z.-G. Chen, *Nano Energy*, 2020, 78, 105379
35. Y. Wang, M. Hong, W.-D. Liu, X.-L. Shi, S.-D. Xu, Q. Sun, H. Gao, S. Y. Lu, J. Zou, Z.-G. Chen, *Chem. Eng. J.*, 2020, 397, 125360
36. M. Tan, X.-L. Shi, W.-D. Liu, M. Li, Y. L. Wang, H. Li, Y. Deng, Z.-G. Chen, *Adv. Energy Mater.*, 2021, 11, 2102578
37. Y. Zhang, G. Xu, J. Mi, F. Han, Z. Wang, C. Ge, *Mater. Res. Bull.*, 2011, 46, 760
38. X. Fan, X. Cai, X. Han, C. Zhang, Z. Rong, F. Yang, G. Li, *J. Solid State Chem.*, 2016, 233, 186
39. M. Scheele, N. Oeschler, I. Veremchuk, K.-G. Reinsberg, A.-M. Kreuziger, A. Kornowski, J. Broekaert, C. Klinker, H. Weller, *ACS Nano*, 2010, 4, 4283
40. C. Zhang, Z. Peng, Z. Li, L. Yu, K. A. Khor, Q. Xiong, *Nano Energy*, 2015, 15, 688
41. M. Hong, Z. Chen, L. Yang, J. Zou, *Nano Energy*, 2016, 20, 144
42. T. Fang, X. Li, C. Hu, Q. Zhang, J. Yang, W. Zhang, X. Zhao, D. J. Singh, T. Zhu, *Adv. Funct. Mater.*, 2019, 29, 1900677
43. H.-J. Zhou, G.-W. Yang, Y.-Y. Zhang, Z.-K. Xu, G.-P. Wu, *ACS Nano*, 2018, 12, 11471
44. A. Kanatzis, C. Papageorgiou, C. Lioutas, T. Kyratsi, *J. Electron. Mater.*, 2013, 42, 1652
45. B. Cai, H.-L. Zhuang, Q. Cao, H. Hu, J. Dong, Asfandiyar, J.-F. Li, *ACS Appl. Mater. Inter.*, 2020, 12, 16426
46. C. Li, S. Ma, P. Wei, W. Zhu, X. Nie, X. Sang, Z. Sun, Q. Zhang, W. Zhao, *Energy Environ. Sci.*, 2020, 13, 535
47. B. Gary, B. Phil, L. Jay, B. Nicholas, M. Michael, B.-C. Avram, Y. Bao, *Nat. Commun.*, 2016, 7, 10302
48. G. E. Bulman, E. Siivola, B. Shen, R. Venkatasubramanian, *Appl. Phys. Lett.*, 2006, 89, 122117
49. D. Singh, A. T. Kutbee, M. T. Ghoneim, A. M. Hussain, M. M. Hussain, *Adv. Mater. Technologies.*, 2018, 3, 1700192
50. Z. Bian, A. Shakouri, *Appl. Phys. Lett.*, 2006, 89, 212101



©2022 The Authors. *Materials Lab* is published by Lab Academic Press. This is an open access article under the terms of the Creative Commons Attribution License, which permits use, distribution and reproduction in any medium, provided the original work is properly cited.